

Charge-Selective, Narrow-Gap Indium Arsenide Quantum Dot Layer for Highly Stable and Efficient Organic Photovoltaics

Youngsang Park, Sung Yong Bae, Taewan Kim, Seongmin Park, Jae Taek Oh, Daekwon Shin, Mahnmin Choi, Hyojung Kim, Bora Kim, Doh C. Lee, Jung Hoon Song,* Hyosung Choi,* Sohee Jeong,* and Younghoon Kim*

The past decade has seen a dramatic surge in the power conversion efficiency (PCE) of next-generation solution-processed thin-film solar cells rapidly closing the gap in PCE of commercially-available photovoltaic (PV) cells. Yet the operational stability of such new PVs leaves a lot to be desired. Specifically, chemical reaction with absorbers via high-energy photons transmitted through the typically-adapted metal oxide electron transporting layers (ETLs), and photocatalytic degradation at interfaces are considered detrimental to the device performance. Herein, the authors introduce a device architecture using the narrow-gap, Indium Arsenide colloidal quantum dots (CQDs) with discrete electronic states as an ETL in high-efficiency solution-processed PVs. High-performing PM6:Y6 organic PVs (OPVs) achieve a PCE of 15.1%. More importantly, as the operating stability of the device is significantly improved, retaining above 80% of the original PCE over 1000 min under continuous illumination, a Newport-certified PCE of 13.1% is reported for nonencapsulated OPVs measured under ambient air. Based on operando studies as well as optical simulations, it suggested that the InAs CQD ETLs with discrete energy states effectively cut-off high-energy photons while selectively collecting electrons from the absorber. The findings of this works enable high-efficiency solution-processed PVs with enhanced durability under operating conditions.


1. Introduction

Next-generation thin-film solar cells composed of solution-processed photovoltaic (PV) absorbers, including lead halide perovskites, organics, and colloidal quantum dots (CQDs), have attracted considerable attention as a promising PV technology for commercialization because of their outstanding PV performances and cost-effective fabrication processes.^[1–7] Yet, the operational stability of such new solar cells leaves a lot to be desired. The operating conditions of continuous 1 sun (AM 1.5G, 100 mW cm⁻²) illumination under ambient air atmosphere often result in degrading the PV absorbers, leading to low device stability.^[8–10] Although many attempts have been made to improve the device stability, such as PV absorber design for high chemical stability, interface engineering, and implementation of a protection layer,^[11–15] solar cells still suffer from low device stability under continuous 1 sun illumination in ambient conditions.

Y. Park, T. Kim, S. Park, D. Shin, M. Choi, B. Kim, S. Jeong
Department of Energy Science
Sungkyunkwan University
2066 Seobu-ro, Jangan-gu, Suwon, Gyeonggi 86582, Republic of Korea
E-mail: s.jeong@skku.edu

Y. Park, D. C. Lee
Department of Chemical and Biomolecular Engineering
Korea Advanced Institute of Science and Technology (KAIST)
291 Daehak-ro, Yuseong-gu, Daejeon 34141, Republic of Korea

S. Y. Bae, J. T. Oh, H. Choi
Department of Chemistry
Research Institute of Convergence of Basic Science, and Institute of Nano Science and Technology
Department of Chemistry
Hanyang University
222 Wangsimni-ro, Seongdong-gu, Seoul 04763, Republic of Korea
E-mail: hschoi202@hanyang.ac.kr

 The ORCID identification number(s) for the author(s) of this article can be found under <https://doi.org/10.1002/aenm.202104018>.

H. Kim, S. Jeong
Artificial Atom and Quantum Materials Center
Sungkyunkwan University
2066 Seobu-ro, Jangan-gu, Suwon, Gyeonggi 86582, Republic of Korea

J. H. Song
Department of Physics
Mokpo National University
1666 Yeongsan-ro, Muan-gun, Jeollanam-Do 58554, Republic of Korea
E-mail: jhsong@mokpo.ac.kr

S. Jeong
SKKU Institute of Energy Science and Technology (SIEST)
Sungkyunkwan University
2066 Seobu-ro, Jangan-gu, Suwon, Gyeonggi 86582, Republic of Korea

Y. Kim
Department of Chemistry
Kookmin University
77 Jeongneung-ro, Seongbuk-gu, Seoul 02707, Republic of Korea
E-mail: younghoon.kim@kookmin.ac.kr

DOI: 10.1002/aenm.202104018

Currently, the efficient and stable solution-processed thin-film solar cells typically employ the wide-bandgap, n-type metal oxide semiconductor electron transporting layers (ETLs), such as ZnO, TiO₂, and SnO₂, on the top of glass/ITO substrates because of their inorganic compound, low work function, high electron mobility, and optical transparency.^[16–19] For example, the inverted device architecture based on metal oxide ETLs in nonfullerene acceptor (NFA)-based organic PVs (OPVs) has very recently led to a significant improvement in PV performance, exceeding power conversion efficiency (PCE) of 18%, and thus received great attention as a promising platform for next-generation eco-friendly thin-film solar cells.^[6,20–23] However, the degradation of organic absorbers under continuous 1 sun illumination in ambient environments often leads to low device stability; for example, PV performance and stability of highly efficient NFA-based OPVs have been only investigated in an inert atmosphere.^[24–26] Currently, the photocatalytic characteristics of metal oxides are considered the main source of the chemical instability of the light-absorbing layer.^[27] Additionally, a large amount of near-ultraviolet (UV) light with high energy, although contributing insignificantly to the collection of charge carriers in solar cells, induces photo-oxidation of OPV absorbers under ambient conditions, resulting in breaking of their chemical bonds.^[28–30]

Herein, we employ narrow-gap electron-accepting layers as an ETL in the way of fabricating high-efficiency solar cells with improved durability. We demonstrate that the use of electron-accepting, narrow-gap indium arsenide (InAs) CQD layer as an ETL in NFA-based bulk-heterojunction (BHJ) OPVs (PM6:Y6 OPVs) results in high-efficiency devices with significantly improved operational stability under continuous 1 sun illumination in ambient air. The InAs CQD-based PM6:Y6 OPVs fabricated in this study exhibit a 15.1% PCE and retain over 80% of the original PCE under continuous 1 sun illumination over 1000 min in ambient conditions. In addition, the non-encapsulated device shows a Newport certified PCE of 13.1% with highly stable current–voltage (*I*–*V*) operation in a quasi-steady-state (QSS) measurement for 9 min under ambient air without device hysteresis. Based on operando studies including femtosecond transient absorption (TA) spectroscopy measurements, we found that the narrow-gap (≈ 1.1 eV) InAs CQDs with discrete and few electronic states can effectively collect only electrons in the new device architecture demonstrated in this study. Furthermore, InAs CQD layers with high absorptivity of near-UV energy effectively block the high-energy photons reaching the PM6:Y6 BHJ absorbers, and thus significantly suppress the photocatalysis at the interface as well as photo-oxidation of the organic moiety.

2. Results and Discussion

2.1. Combination of Narrow-Gap InAs CQD layers with a BHJ

We employed PM6:Y6 OPVs based on the inverted device architecture of glass/ITO/ZnO ETL/PM6:Y6 BHJ/MoO_x/Ag as a control device, which has been considered to provide better device stability under operating conditions with a PV performance exceeding a 15% PCE (Figure 1a).^[6,20,31,32] The ZnO metal oxide has a high density of surface and internal defects

corresponding to non-lattice oxygen and oxygen vacancies, which gives rise to a photocurrent upon UV light illumination.^[33,34] At the same time, wide-bandgap and oxygen-deficient ZnO has a deep valence band (VB) position enabling redox reactions with oxygen and moisture under ambient conditions and thus has an inherent photocatalytic property.^[27] In addition, the large number of high-energy photons in near-UV light, after passing through the highly transparent ZnO ETLs, triggers the photo-oxidation by reacting with oxygen in ambient air.^[28] These photocatalytic effects and photo-oxidation are known to subsequently decompose conjugated chain molecules in BHJ absorbers, leading to low device stability of PM6:Y6 OPVs under 1 sun illumination in ambient air (Figure 1a).^[27,28,35–38]

The quest for new inorganic ETLs led us to employ electron-accepting InAs CQDs, which have recently been developed in terms of synthesis and various optoelectronic applications.^[39,40] We expect that the use of InAs CQDs having a much shallower highest quantized state of the VB ($1S_h$) and a narrower gap than ZnO might prevent the redox reaction (i.e., photocatalytic reaction) with oxygen and moisture species under ambient conditions (Figure 1a).^[41–43] Also, narrow-gap InAs CQDs absorb high-energy photons in near-UV light (Figure S1, Supporting Information) and may suppress the photo-oxidation of the BHJ absorber layer that occurs under ambient air. However, when the narrow-gap semiconductors are employed as an ETL in solar cells, it might be difficult to selectively collect the charge carriers (i.e., electrons and holes) generated from the relatively large-gap PV absorbers, because of unfavorable energy level alignment (Figure S2, Supporting Information). That is, the $1S_h$ of InAs CQD ETL is shallower than the highest occupied molecular orbital (HOMO) of PM6:Y6 BHJ absorber; thus both electrons and holes generated from BHJ absorber could transfer to InAs CQD ETLs. Here, we found that the presence of abundant electrons in narrow-gap InAs CQDs with discrete and few electronic states could suppress the charge transfer of holes and thus might enable the charge-selective collection, as will be discussed in Figures 3 and 5 in detail.

To investigate the optical absorption of each layer affecting the device performance, we first measured the UV–Vis–NIR absorption spectra of the ZnO, InAs CQD, and PM6:Y6 BHJ films fabricated with the real thicknesses, which were used in the OPV device, on bare glass substrates and then plotted them along with the 1 sun spectrum (Figure 1b). The BHJ films show two strong absorption bands at approximately 600 and 800 nm, corresponding to polymer donor PM6 and NFA Y6, respectively, which are dominantly attributed to the photo-generation of electron and hole pairs in the absorber layer. The wide-bandgap ZnO film is highly transparent to solar light over the entire range of UV–Vis–NIR to near-infrared. The 20-nm-thin narrow-gap InAs CQD film shows an overall higher absorption than ZnO, especially in the high-energy area, yet does not intervene BHJ absorption significantly.

We then fabricated inverted PM6:Y6 OPVs based on the respective ZnO and InAs CQD ETLs and investigated the photo-stability of each 5 high-efficiency device under continuous 1 sun illumination in ambient air while irradiating light through the glass substrate (Figure 1c). We confirmed using the atomic force microscopy (AFM) measurements that there were no morphological changes of PM6:Y6 BHJ thin-films fabricated

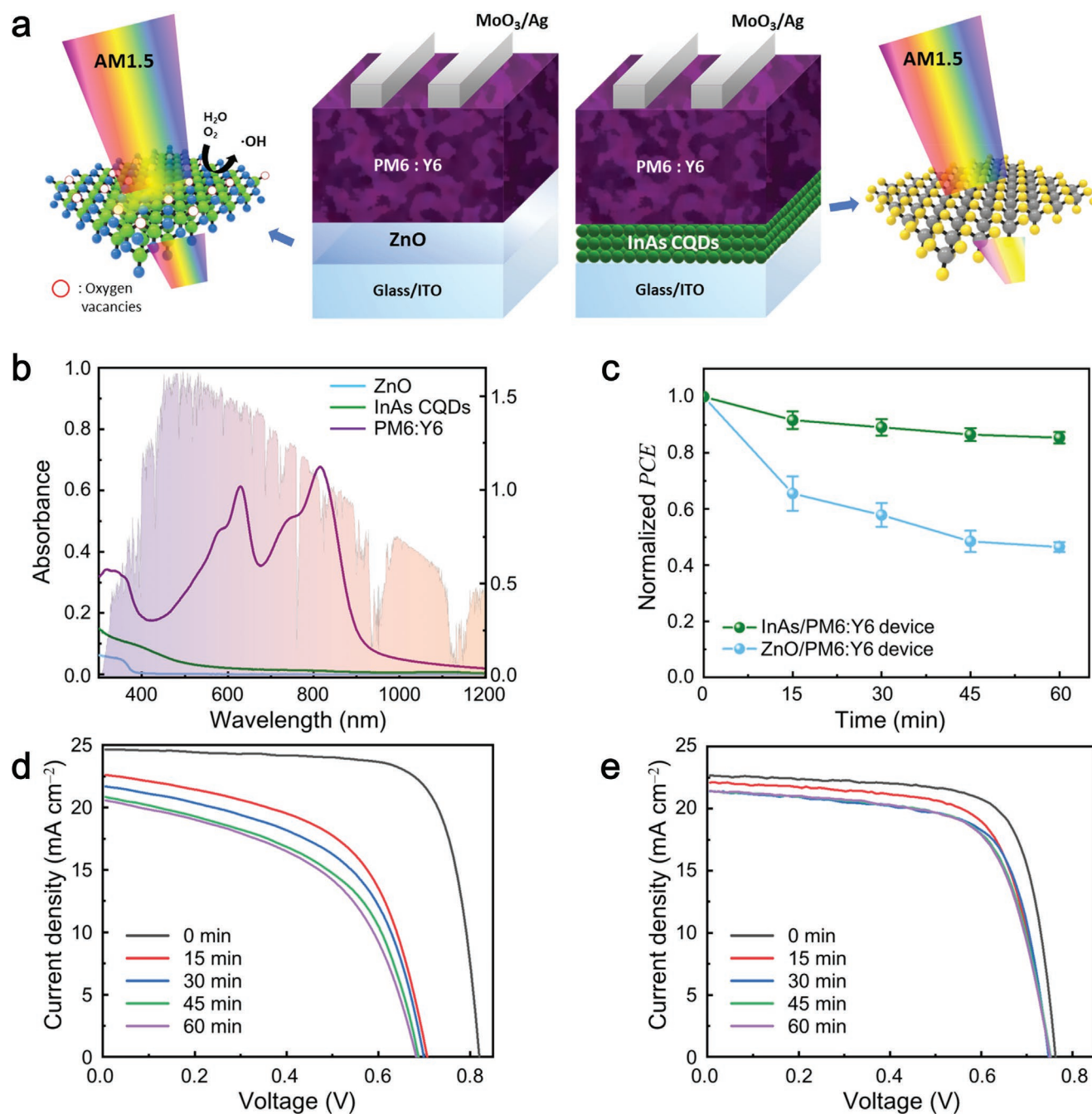


Figure 1. Air- and photo-stable PM6:Y6 OPVs based on the InAs CQD ETL. a) Schematic illustrations of the PM6:Y6 OPVs based on the respective ZnO (left) and InAs CQD (right) solids as an ETL, and crystal structure of ZnO and InAs CQDs. b) Absorbance spectra of ZnO, InAs CQD, and the PM6:Y6 BHJ absorber along with the 1 sun solar spectrum. c) Photo-stability of each 5 devices for PM6:Y6 OPVs based on the respective ZnO and InAs CQD ETLs under continuous 1 sun illumination in ambient air. d,e) Evolution of the *J*-*V* characteristics of PM6:Y6 OPVs based on the ZnO (d) and InAs CQD (e) ETLs under continuous 1 sun illumination, which is used to plot the graph in (c).

onto the ZnO and InAs CQD ETLs (Figure S3, Supporting Information). The best-performing PM6:Y6 OPVs based on the ZnO and InAs CQD ETLs showed the initial PCE of 15.3 and 12.7%, respectively (Table 1). We also provide the PV performance parameters of all devices, which are used to investigate the photo-stability in Figure 1c (Table S1 and S2, Supporting Information). While the PCE of the control device decreased to

less than 50% of the initial value in 60 min under continuous 1 sun illumination, the PCE of the device based on the InAs CQD ETL remained high, retaining over 85% of the initial PCE.

We also investigated the photo-stability of the devices by illuminating under an inert N₂ condition, which has been generally tested in OPVs (Figure S4 and Table S3, Supporting Information). The device based on the InAs CQD ETL

Table 1. PV parameters of the PM6:Y6 OPVs based on the ZnO, InAs CQD, and InAs CQD@ZnO ETLs (In-lab PCE).

Device		V_{oc} [V]	J_{sc} [mA cm^{-2}]	FF	PCE [%]
ZnO	Champion	0.82	24.6	0.76	15.3
	Average	0.82 ± 0.02	23.8 ± 0.65	0.75 ± 0.01	14.5 ± 0.43
InAs CQD	Champion	0.76	22.6	0.74	12.7
	Average	0.75 ± 0.01	22.9 ± 0.56	0.70 ± 0.01	12.2 ± 0.27
InAs CQD@ZnO	Champion	0.83	24.5	0.75	15.1
	Average	0.82 ± 0.02	23.8 ± 0.47	0.73 ± 0.01	14.3 ± 0.41

illuminated for 60 min under an inert N_2 condition preserved the initial PCE up to 96%, which is higher than that of illuminated under ambient air. The photo-stability of control device based on the ZnO ETL illuminated under an inert N_2 condition was also improved; however, it was much lower than the photo-stability of the device based on InAs CQD ETL illuminated under an inert N_2 condition as well as ambient air. These results suggest that narrow-gap InAs CQD ETL can further enhance the photo-stability of NFA-based OPVs, along with the encapsulation technology, which is necessary for large-scale production and commercial application.

Figure 1d,e shows the evolution of the current density–voltage (J – V) curves of each best-performing device over time, which were used to plot the graph in Figure 1c. The severe drop in PCE in the control device resulted from the reduction in the PV performance parameters including open-circuit voltage (V_{oc}), current density (J_{sc}), and fill factor (FF) with increasing 1 sun illumination time (Table S1, Supporting Information). On the other hand, the device based on the InAs CQD ETL showed negligible degradation of the J – V curve with continuous 1 sun illumination. We also monitored the dark and ambient storage stability and found that the device based on the InAs CQD ETL retained over 95% of the original efficiency for over 200 h (Figure S5, Supporting Information).

2.2. Air- and Photo-stabilities of the PM6:Y6 BHJ Absorber

To specify the origin of the efficiency decrease over time upon illumination, we first investigated the photo-stability of PM6:Y6 BHJ films fabricated on metal oxide- and InAs CQD-coated glass substrates. We also investigated SnO_2 metal oxide, which is known to improve the device stability of inverted PM6:Y6 OPVs under inert N_2 conditions.^[44–46] We measured the absorbance changes before and after exposure to 1 sun illumination under ambient air for different times and found absorbance of the BHJ film fabricated on the glass/ZnO substrate significantly decreased. Although the SnO_2 ETL improved the device stability under inert N_2 conditions,^[46] we still observed a significant decrease in the absorbance of the PM6:Y6 BHJ film illuminated in ambient air. On the contrary, the absorbance feature of the PM6:Y6 BHJ film fabricated on the glass/InAs CQD substrates did not change over time regardless of 1 sun exposure in ambient air (Figure 2a and Figure S6, Supporting Information). We also confirmed using Fourier-transform infrared

(FT-IR) measurements that the PM6:Y6 BHJ film on the glass/InAs CQD substrate was highly photo-stable, as the IR signals corresponding to donor PM6 and NFA Y6 after 1 sun illumination remained the same (Figure S7, Supporting Information).^[22,47] In the case of ZnO and SnO_2 , the decomposition of conjugated chain molecules in PM6 and Y6 was indicated by the decrease in IR signal intensity. These results indicate that the chemical bonds in conjugated chain molecules are decomposed by superoxide radical ions and high-energy photons.^[27,48]

Based on the absorption spectra in Figure 2a, we plotted the absorbance changes of NFA Y6 on each substrate as a function of 1 sun illumination time under ambient air because the photo-degradation of NFA Y6 is more pronounced (Figure 2b).^[27] Although wider-bandgap metal oxide SnO_2 is known to have a much lower photocatalytic property than ZnO,^[44–46] a decrease in the absorbance of NFA Y6 on SnO_2 with increasing illumination time was still observed. In particular, ZnO, which has a higher photocatalytic power and transmits lesser high-energy photons (i.e., induces less photo-oxidation) than SnO_2 (Figure S8, Supporting Information), led to the most significant decrease in the absorbance of NFA Y6, suggesting that the photocatalytic effect influences the degradation of NFA Y6 more than photo-oxidation. In addition, we plotted the absorbance changes of donor PM6 based on the absorbance spectra in Figure 2a. Although it was less than that of NFA Y6, we confirmed that the absorbance of donor PM6 on ZnO and SnO_2 also decreased (Figure S9, Supporting Information).

Although the photocatalytic effect is dominant, we cannot exclude the degradation of NFA Y6 and donor PM6 due to photo-oxidation by high-energy photons. We thus investigated the photo-stability of the BHJ film prepared on a bare glass substrate (Figure S10, Supporting Information). Even without photocatalytic ZnO or SnO_2 metal oxides, decomposition of the BHJ absorber still occurred, suggesting that photo-oxidation should also be suppressed to achieve an air- and photo-stable NFA-based BHJ absorber under 1 sun illumination in ambient conditions. Indeed, our narrow-gap InAs CQDs effectively suppress both the photocatalytic effect and photo-oxidation, resulting in no absorbance change of NFA Y6 and donor PM6 under continuous 1 sun illumination in ambient air for 90 min.

Considering that the PM6:Y6 BHJ thin-films were decomposed both by the photocatalytic effect and photo-oxidation, the UV filter might be suggested to block the high-energy photons in near UV light at the source. Indeed, PM6:Y6 BHJ OPV based on the ZnO ETL with the UV filter is stable under 1 sun illumination in ambient air. However, at the same time, a significant loss in PV performance was observed because the UV filter completely blocked the UV light needed for the high-current level of ZnO ETLs necessary for efficient electron extraction (Figure S11 and Tables S4 and S5, Supporting Information).^[49] Further interface engineering strategies on ZnO layer^[24,50] were attempted and resulted in improving the photo-stability; however, we found that the PM6:Y6 BHJ thin-films still decomposed under 1 sun illumination in ambient air mainly because of the transmission of high-energy photons (i.e., photo-oxidation) (Figure S12, Supporting Information).

Chemisorbed oxygen ions (i.e., O_2^-) on the oxygen-deficient surface of metal oxides can be desorbed via the recombination of the photo-generated holes with the electrons of oxygen ions

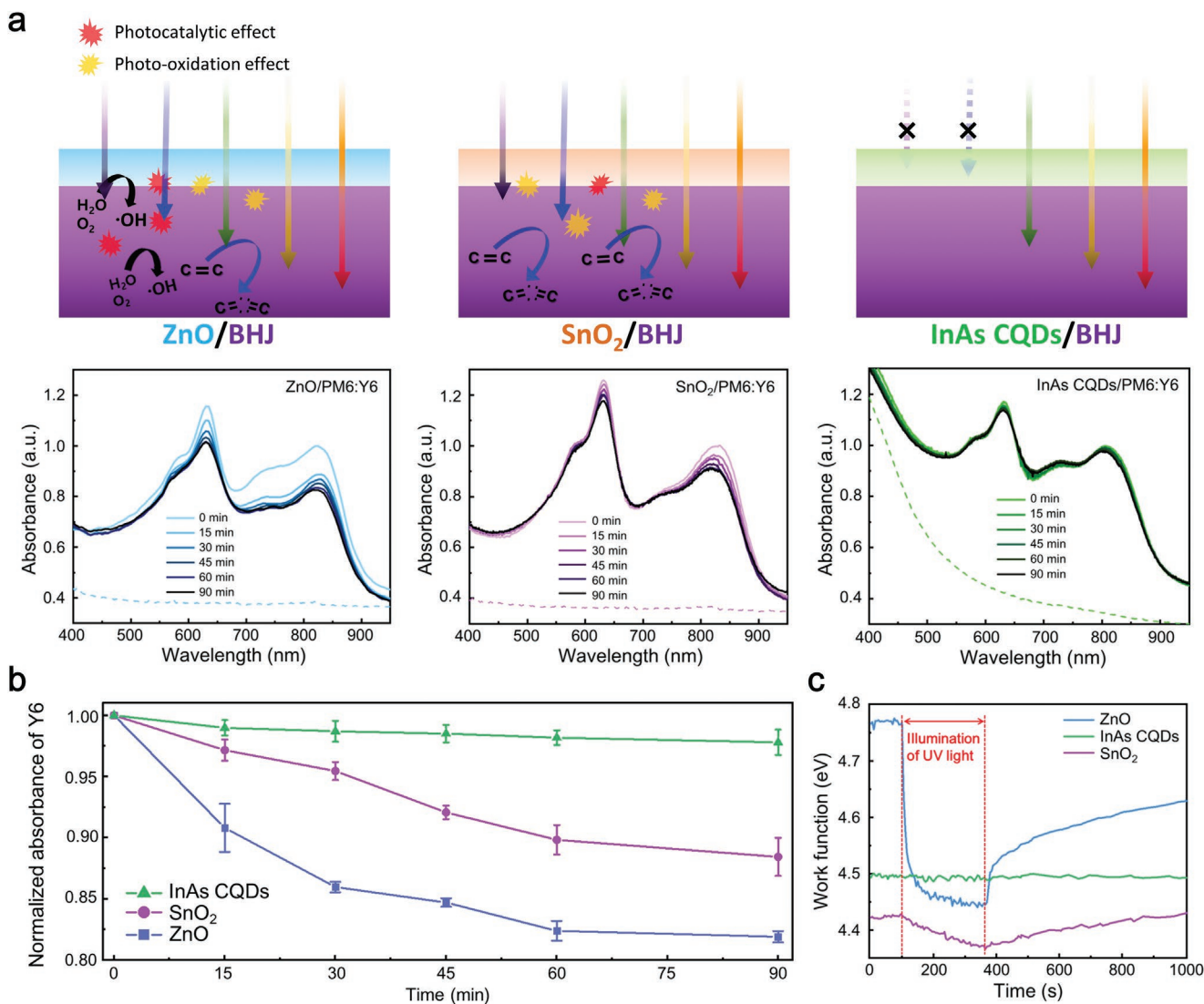


Figure 2. Air- and photo-stability of PM6:Y6 BHJ absorbers on the various ETLs. a) Schematic illustrations, and absorbance spectra of PM6:Y6 BHJ absorbers on glass/ZnO, glass/SnO₂, and glass/InAs CQD substrates as a function of the 1 sun illumination time under ambient air. The dashed lines in each graph indicate the absorbance spectra of glass/each ETL with the absence of PM6:Y6 BHJ absorbers. b) Absorbance changes of NFA Y6 on each substrate as a function of the 1 sun illumination time under ambient air. c) Work function shift of ZnO, SnO₂, and InAs CQD solids under ambient air with and without UV light exposure.

and result in a work function shift. We carried out Kelvin probe measurements to investigate the work function shifts of ZnO, SnO₂, and InAs CQD solids under ambient air with and without UV light exposure (Figure 2c).^[51,52] The initial work function of ZnO was obtained using Kelvin probe measurements, with a value of 4.77 eV. When ZnO was illuminated with UV light, the work function of ZnO significantly decreased to 4.45 eV because of the charge redistribution resulting from the desorption of the chemisorbed oxygen ions on the ZnO surfaces.^[52,53] After turning off the UV light, the work function began to increase over time, possibly due to the re-absorption of oxygen ions on the ZnO surfaces under ambient air. In the case of less photocatalytic SnO₂, the overall change in work function was much less than that of ZnO but still occurred. However, InAs CQD solids showed a constant work function of 4.50 eV regardless

of UV light exposure under ambient air, suggesting that InAs CQDs effectively suppressed the photocatalytic properties.

Further to confirm the generality of our strategy based on the narrow-gap InAs CQD ETLs, we employed ITIC and Y7, which are other types of NFAs with different molecular structures and energy levels, and investigated the PV performance and photo-stability of PM6:ITIC and PM6:Y7 BHJ OPVs based on the ZnO and InAs CQD ETLs, respectively.^[27,53–55] As demonstrated in the PM6:Y6 BHJ OPVs, the PM6:ITIC and PM6:Y7 BHJ OPVs based on the narrow-gap InAs CQD ETLs showed the initial PCE of 7.1% and 11.4%, respectively, and their photo-stability under continuous 1 sun illumination in ambient air significantly improved compared to those of the wide-bandgap ZnO ETLs (Figures S13 and S14 and Tables S6 and S7, Supporting Information).

2.3. Charge Transfer Dynamics between the InAs CQD Solids and the PM6:Y6 BHJ

To investigate the charge transfer characteristics in our OPV device architecture using narrow-gap InAs CQD ETL, we performed femtosecond TA spectroscopy measurements. For this investigation, we fabricated the PM6, Y6, PM6:Y6 BHJ, ZnO/PM6:Y6 BHJ, and InAs CQD/PM6:Y6 BHJ onto the quartz substrates and analyzed their respective charge transfer dynamics. Based on the absorption bands of PM6 and Y6 (Figure S15, Supporting Information), it has been known that the negative bleaching signals are generally observed at 580 and 632 nm for PM6 and 850 nm for Y6, respectively.^[22] Since narrow-gap InAs CQDs also have the bleaching signal in near-infrared region, we decided to monitor the decay kinetics in visible range. As expected, TA results showed the negative photobleaching signals at 580 and 632 nm for PM6, which increase as a function of time delays, while the changes in photobleaching signal are negligible for Y6 (Figure S16, Supporting Information). When we measured TA spectra of PM6:Y6 BHJ, we found the shape of TA signals identical to that of PM6 (Figure 3a), but for the decay kinetics, the bleach of PM6:Y6 BHJ was recovered faster than the that of PM6 at early times, specifically within 10 ps (Figure 3b). We believe that the fast decay dynamics originated from the electron transfer process from PM6 to Y6. In addition, the increase in bleach of PM6:Y6 BHJ at the time delay up to 100 ps is considered as the hole transfer process from Y6 to PM6 (Figure 3b). These results confirm that the PM6 and Y6 blended in BHJ efficiently act as a donor and acceptor, respectively.

To examine the changes in carrier dynamics of PM6:Y6 BHJs onto each ETL, we extracted the decay components of PM6:Y6 BHJ, ZnO/PM6:Y6 BHJ, and InAs CQD/PM6:Y6 BHJ at 632 nm from TA spectra (Figure 3c,d) using a multiple exponential function (Figure S17, Supporting Information) and summarized the results in Figure 3e. PM6:Y6 BHJ showed a fast component (τ_1) of 0.47 ps and a slow component (τ_2) of 11.05 ps, corresponding to exciton dissociation and charge transfer time, respectively. The excitons generated in PM6:Y6 BHJ dissociate at the donor-acceptor interface within 1 ps, and the charge carriers transfer to donor PM6 and acceptor Y6 or additional charge transfer states in less than 15 ps.^[56,57] The τ_2 value of ZnO/PM6:Y6 BHJ and InAs CQD/PM6:Y6 BHJ significantly decreased up to 4.79 and 6.70 ps, respectively, which are much faster than that of PM6:Y6 BHJ. In addition, through the result that the τ_2 of ZnO/PM6:Y6 BHJ was faster than that of InAs CQD/PM6:Y6 BHJ, it might be concluded that charge transfer of ZnO/PM6:Y6 BHJ is more efficient than that of InAs CQD/PM6:Y6 BHJ, which is consistent with that of the PV performance of each device (Figure 1d,e).

Since the highest occupied state of InAs CQDs is higher than that of PM6:Y6 BHJ, additional pump-dependent TA measurements were carried out to see if hole transfer can occur in InAs CQD/BHJ (Figure S18, Supporting Information). We excited only Y6 using 750 nm (1.65 eV) pump wavelength and compared the decay kinetics of PM6, PM6:Y6 BHJ, and InAs CQD/PM6:Y6 BHJ at 580 nm (Figure 3f). The PM6 did not show any bleach signal; however, the bleach signal increased up to 100 ps in PM6:Y6 BHJ due to the hole transfer from

Y6 to PM6. Surprisingly, InAs CQD/PM6:Y6 BHJ showed an increase in the bleach signal, indicating that holes did not further transfer to the InAs CQD ETL. The electronic states of CQDs are discrete and sparse at the quantized energy band, and further, the InAs CQDs have the intrinsic electron-donating surface structure, which makes holes scarcely reside. Consequently, we believe that our narrow-gap InAs CQDs can selectively collect the charge carriers (i.e., electrons).

2.4. Optical Simulation of Light Absorption and Photocurrent Generation in ETLs and BHJ

The use of narrow-gap ETL certainly enhanced the photostability of device, yet the light absorption of the narrow-gap ETL may adversely affect the device performance of solar cells. It is thus in due course we model and calculate the light absorption of each layer in these device structures using the transfer matrix method (TMM), which provides powerful predictions for investigation of the light path and absorption inside a device structure.^[58,59] Figure 4a,b show the distribution spectra of the light intensity fraction absorbed by ETLs (i.e., ZnO and InAs CQDs) and PM6:Y6 BHJ layers in the respective OPV devices based on ZnO and InAs CQD ETLs (solid lines) and their accumulated photocurrent (J_{ph}) calculated from the TMM results under 1 sun conditions (dashed lines). The J_{ph} obtained by the TMM simulation is different from the J_{SC} obtained by the J - V measurement of solar cells because the internal quantum efficiency is assumed to be 100% in the TMM simulation.

In the case of the device based on the ZnO ETL, the J_{ph} generated in the PM6:Y6 BHJ layer (29.8 mA cm^{-2}) mainly contributes to the J_{SC} of the device, obtained from the J - V and external quantum efficiency (EQE) measurements, because the light intensity fraction absorbed by the wide-bandgap and highly-transparent ZnO ETL is too low to generate a J_{ph} (Figure 4a). However, the device based on the InAs CQD ETL has two different absorbing layers contributing to the generation of a J_{ph} : the PM6:Y6 BHJ and InAs CQD layers absorb light and generate J_{ph} of 26.9 and 2.4 mA cm^{-2} , respectively (Figure 4b). To investigate the effect of InAs CQD absorption on the J_{SC} in the solar cell based on the InAs CQD ETL, EQE spectra of each device were measured (Figure S19, Supporting Information). We found that the solar cell based on the InAs CQD ETL shows a lower EQE in the wavelength range of less than 600 nm than the solar cell based on the ZnO ETL. Therefore, the J_{SC} calculated from the EQE spectrum of the solar cell based on the InAs CQD ETL (22.3 mA cm^{-2}) was lower than that of the solar cell based on the ZnO ETL (24.3 mA cm^{-2}). In other words, the J_{ph} generated by the light absorption of the InAs CQD layer did not contribute to the J_{SC} in solar cells, but rather caused a slight reduction in J_{ph} and J_{SC} , which can be caused by the light absorption of the PM6:Y6 BHJ.

Although the device stability of OPVs based on the InAs CQD ETL under continuous 1 sun illumination in ambient air was significantly improved, the light absorption and J_{ph} of the InAs CQD layer led to a reduction in the J_{SC} of the resultant solar cells, indicating a trade-off relationship between light absorption and device performance. To investigate the light absorption of the InAs CQD layer affecting the J_{SC} in the PM6:Y6 BHJ

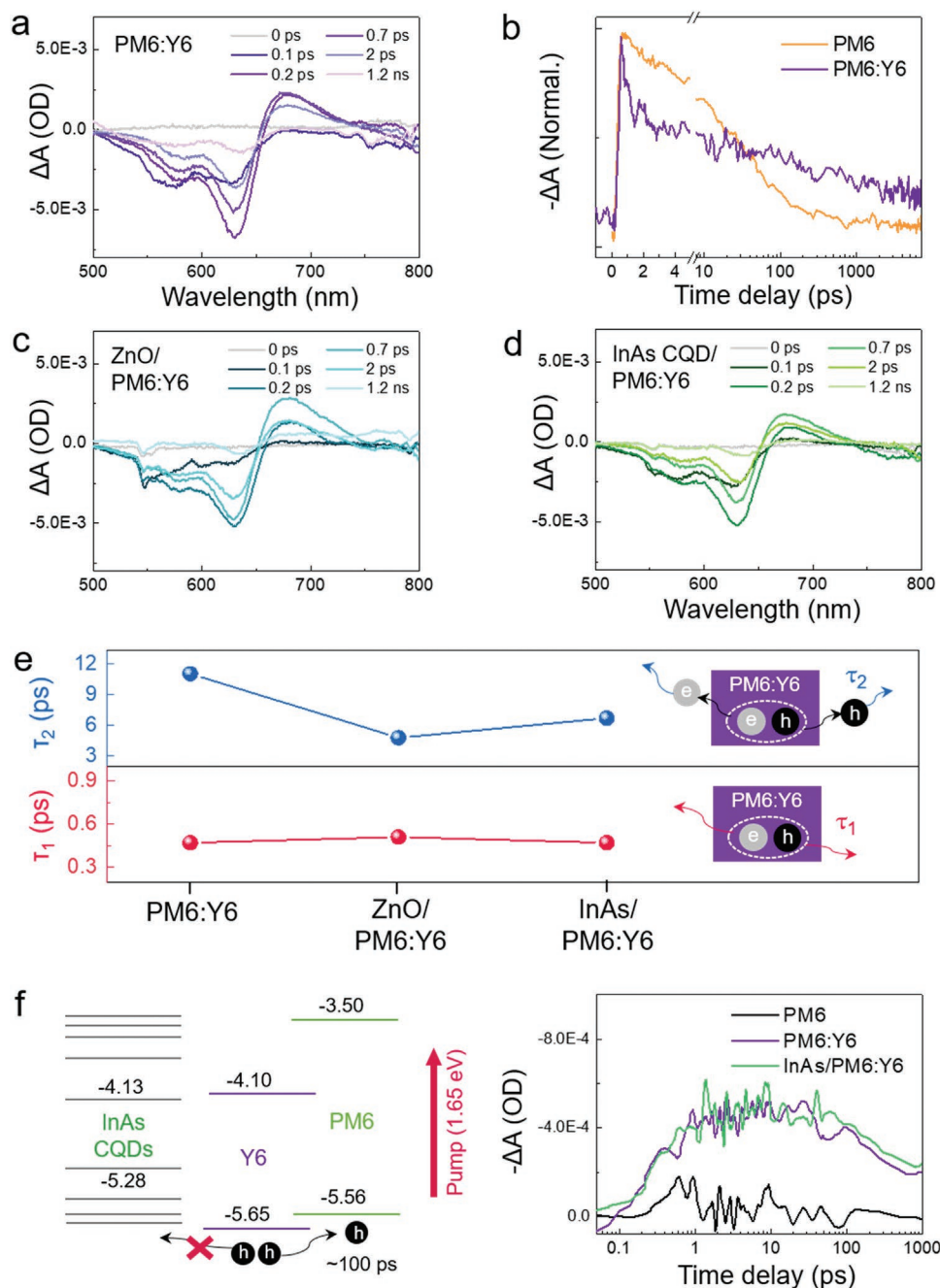


Figure 3. Charge transfer mechanism in InAs CQD/BHJ. a) TA spectra of the PM6:Y6 BHJ film at the different time delays. b) TA decay kinetics of the PM6 and PM6:Y6 BHJ films at 632 nm showing the electron and hole transfer process, respectively. c) d, TA spectra of c) ZnO/PM6:Y6 and d) InAs CQD/PM6:Y6 films at the different time delays, respectively. e) Exciton dissociation (τ_1) and carrier transfer (τ_2) time obtained through multiple exponential fitting for different structures. f) Energy level diagram depicting the hole transfer process and TA decay kinetics of PM6, PM6:Y6, and InAs CQD/PM6:Y6 at 580 nm under 750 nm (1.65 eV) excitation, respectively.

OPV based on the InAs CQD ETL in detail, we calculated the J_{ph} of the PM6:Y6 BHJ absorbers in each device based on the respective ZnO and InAs CQD ETLs for different film thicknesses of each ETL and then compared these values to the J_{SC} obtained from each optimized device, presented in Figure 1. Figure 4c shows the changes in the calculated J_{ph} with the film thickness of each ETL, generated by the PM6:Y6 BHJ layer in each device based on the respective ZnO and InAs CQD ETLs.

The J_{ph} of the PM6:Y6 BHJ layer in the device based on the InAs CQD ETL was overall lower than that in the device based on the ZnO ETL and particularly decreased with increasing film thickness of the InAs CQD ETL. Although the InAs CQD ETL produces an additional J_{ph} , confirmed by TMM simulation, the optimal J_{SC} (24.8 mA cm^{-2}) of the device based on the ZnO ETL with an approximately 30-nm-thick ZnO ETL was higher than that (22.6 mA cm^{-2}) of the device based on the InAs CQD ETL

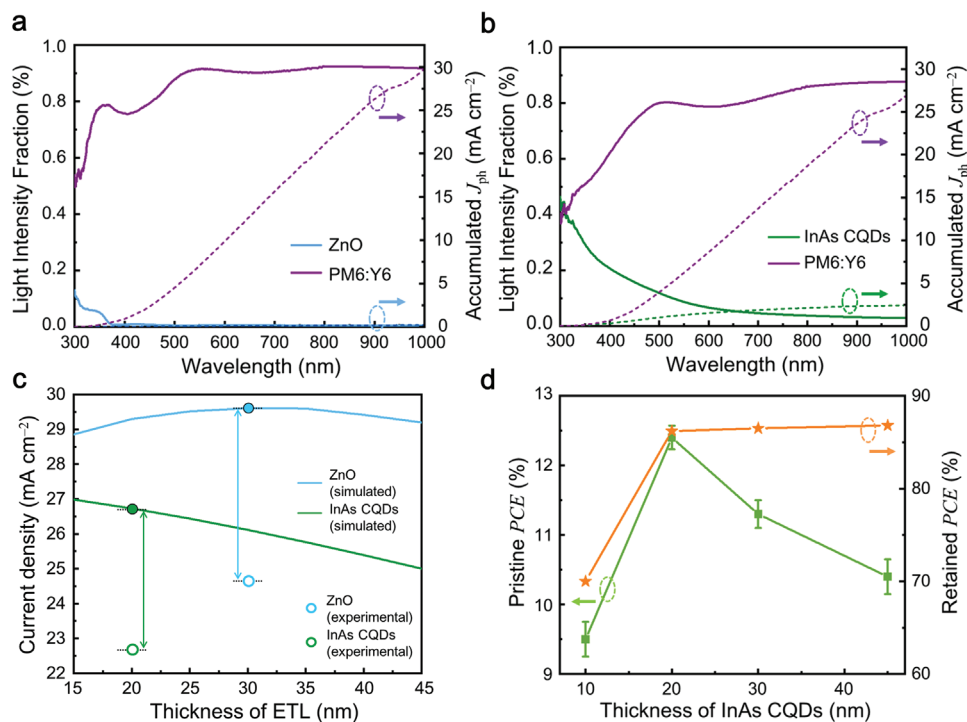


Figure 4. Optical simulation of each device structure. a,b) Simulated light absorption (solid lines) and accumulated J_{ph} (dashed lines) curves of each ETL and PM6:Y6 absorbers in OPVs based on the respective ZnO and InAs CQD ETLs under 1 sun illumination. c) J_{ph} generated by the PM6:Y6 absorber in OPVs based on the respective ZnO and InAs CQD ETLs with different film thicknesses of each ETL. Unfilled circles indicate the experimental J_{SC} obtained from J - V measurements of the optimized OPVs with the respective ZnO and InAs CQD ETLs. d) PCE and photo-stability of PM6:Y6 BHJ OPVs with different film thicknesses of the InAs CQD ETL under 1 sun illumination in ambient air.

with an approximately 20-nm-thick InAs CQD ETL (Figure S20, Supporting Information).

We also fabricated solar cells based on the InAs CQD ETL with different film thicknesses of InAs CQD ETLs and investigated their J - V curves and photo-stability under continuous 1 sun illumination to clarify the effects of the InAs CQD ETL on the device performance and stability (Figure 4d). The film thicknesses of the InAs CQD ETLs were controlled by varying the solution concentration of InAs CQDs in dimethylformamide (DMF) solvent from 30 to 100 mg mL⁻¹ and confirmed using AFM (Figure S20, Supporting Information). We found that the device performance of the OPVs based on the InAs CQD ETL increased with increasing film thickness up to approximately 20 nm, achieving increases in the FF and shunt resistance of the device (Figure S21, Supporting Information). However, a further increase in the film thickness of the InAs CQD layers resulted in decrease in the device performance, especially J_{SC} , because the high loading amount of InAs CQDs led to a reduction in the light absorption of the PM6:Y6 BHJ absorber (Table S8, Supporting Information). Although the device performance decreased, the OPVs based on the InAs CQD ETL were highly photo-stable under continuous 1 sun illumination in ambient air and maintained over 85% of their initial performance with increasing film thickness of the InAs CQD ETL because of their effective blocking of high-energy photons (Table S9, Supporting Information). This result indicates that an optimal thickness of narrow-gap InAs CQD ETLs is required for simultaneously improving device performance and photo-stability.

2.5. Characterization of Solar Cells

In the absence of ETL, both the electrons and holes from the PV absorber layer would recombine at the transparent electrode (i.e., ITO and FTO).^[60] To effectively prevent the charge carrier recombination and selectively extract the charge carriers by charge carrier drift mechanism, wide-bandgap ETLs (i.e., ZnO), which have a favorable and sufficient energy level offset with PV absorber, have been widely employed in solar cells. The use of narrow-gap semiconductor as ETL may easily create a situation in which electron and hole recombination are promoted. Here, we designed the new ETL architecture with tuned density of states via quantization as the lowest quantized state of the conduction band ($1S_e$) of narrow-gap InAs CQDs similar with the lowest unoccupied molecular orbital (LUMO) of Y6. Indeed, selective collection of charge carriers based on the charge carrier diffusion mechanism was successfully demonstrated. We suggest that the selective electron diffusion in InAs CQD ETLs is originated from the concentration graded electrons at the interface of Y6/InAs CQD and the low probability of hole formation in the InAs CQDs due to the discrete and few electronic states at the quantized energy bands.

The use of narrow-gap InAs CQD ETLs in PM6:Y6 BHJ OPVs results in a dramatic improvement in the photo-stability of the device under ambient conditions; however, the PV performance of ZnO ETL-based OPVs is higher than that of InAs CQD ETL-based OPVs. The charge carriers separated from the excitons of BHJ transfer to ZnO ETL faster than InAs CQD

ETL, as confirmed in TA analysis (Figure 3). This result limits the charge carrier extraction of the new PM6:Y6 OPV architecture, resulting in the charge carrier recombination, which affects the reduction in V_{OC} and J_{SC} in the solar cells. Furthermore, the PV performance with InAs CQD ETLs inevitably decreases due to the reduction in the amount of light reaching the PM6:Y6 BHJ absorber. Therefore, the best-performing PM6:Y6 BHJ OPV based on the InAs CQD ETL, measured under ambient conditions without encapsulation, showed a PCE of 12.7% with a V_{OC} of 0.76 V, a J_{SC} of 22.6 mA cm^{-2} , and a FF of 0.74, which is overall lower than the performance of the ZnO ETL with a PCE of 15.3%, a V_{OC} of 0.82 V, a J_{SC} of 24.6 mA cm^{-2} , and a FF of 0.76 (Figure 5a and Table 1). In addition, we found that the reduction in V_{OC} of PM6:Y6 BHJ OPV based on the InAs CQD ETL is due to the direct contact with InAs CQD and PM6 (Figure S22, Supporting Information).^[61–63] The charge carrier recombination can be occurred at the interface between donor PM6 and InAs CQD ETL because the $1S_h$ and $1S_e$ of InAs CQDs are shallower and deeper than HOMO and LUMO of donor PM6, respectively, as confirmed in Figure S2, Supporting Information. To further improve the PV performance of OPVs based on the InAs CQD ETL while retaining their high photo-stability, we devised bi-layered ETLs composed of InAs CQDs on ZnO (InAs CQD@ZnO). We also confirmed that the bi-layered InAs CQD@ZnO ETL showing the best PV performance in this strategy shows the film thickness of approximately 50 nm, corresponding to the sum of the

respective film thickness of ZnO (approximately 30 nm) and InAs CQD (approximately 20 nm) ETLs (Figures S20 and S23, Supporting Information). The bi-layered InAs CQD@ZnO ETL effectively suppresses not only the photocatalytic reaction by avoiding interfacial contact between ZnO and the PM6:Y6 BHJ absorber due to the densely-packed InAs CQDs (Figure S24, Supporting Information) but also the photo-oxidation by blocking the high-energy photons from reaching the absorber layer due to the narrow-gap InAs CQDs. In addition, as the film thickness of InAs CQD layer increased, the combined energy level of bi-layered InAs CQD@ZnO ETL shifted toward vacuum level due to the interfacial dipole moment between the InAs CQD and ZnO layers, allowing favorable charge transfer (Figure S25, Supporting Information).^[64,65] When InAs CQD layer is thicker than 20 nm, however, light absorption is reduced as mentioned in Figure 4. Therefore, the favorable energy level alignment, the protection of high energy photons, and the optimal charge transport are achieved at 20 nm InAs CQD layer thickness. Thus, the PV performance of PM6:Y6 OPV based on the bi-layered InAs CQD@ZnO ETL was improved up to a PCE of 15.1% with a V_{OC} of 0.83 V, J_{SC} of 24.5 mA cm^{-2} , and a FF of 0.75 (Figure 5a and Table 1). We also confirmed using EQE spectrum measurement that the ability of charge carrier extraction in PM6:Y6 OPV based on the bi-layered InAs CQD@ZnO ETL was improved (Figure S26, Supporting Information). Device histograms of the PV performance for all 48 solar cells are presented to demonstrate the reproducibility of the results

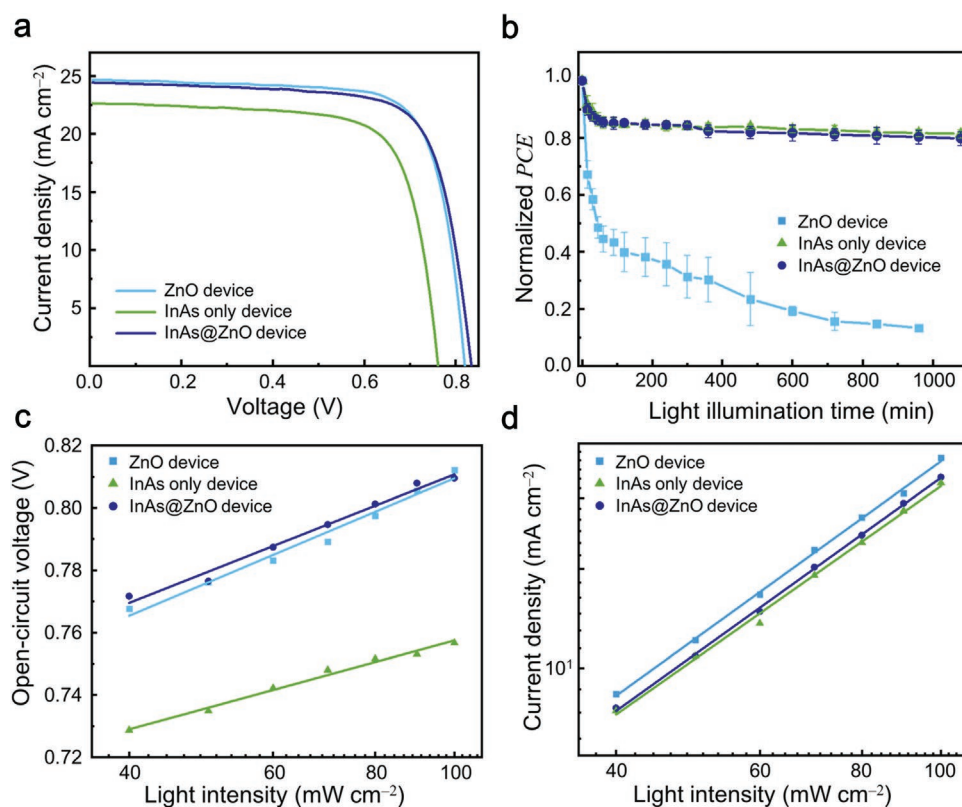


Figure 5. Device characteristics. a) J – V curves of the best-performing PM6:Y6 BHJ OPVs based on the respective ZnO, InAs CQD, and InAs CQD@ZnO ETLs, measured under 1 sun illumination in ambient air without encapsulation. b, Long-term device stability of each 5 devices for PM6:Y6 BHJ OPV under continuous 1 sun illumination in ambient air. c, d, Incident light intensity-dependent V_{OC} (c), and J_{SC} (d) of each PM6:Y6 BHJ OPV.

(Figure S27, Supporting Information). In addition, the nonencapsulated PM6:Y6 BHJ OPVs based on the InAs CQD@ZnO ETL produced a certified PCE of 13.1% and showed highly stable $I-V$ operation in a QSS measurement for 9 min under ambient air without device hysteresis (Figures S28 and S29, Supporting Information).

We investigated the device stability of each 5 high-efficiency nonencapsulated OPVs based on the respective ZnO, InAs CQD, and InAs CQD@ZnO ETLs under continuous 1 sun illumination in ambient air over 1000 min while irradiating the light through the glass substrates (Figure 5b). As discussed in relation to Figure 1c, the PV performance of the control OPVs based on the ZnO ETL significantly decreased to less than 50% of the initial value in 60 min and further decreased to less than 20% of the initial value in 1000 min. In addition, several control devices did not operate at all after 1 sun illumination for 600 min (Figure 5b and Table S10, Supporting Information). However, the PV performance of the OPVs based on the InAs CQD ETL remained high above 80% of the initial value for over 1000 min (Figure 5b and Table S11, Supporting Information). The OPVs based on the InAs CQD@ZnO ETL also retained over 80% of the initial PV performance for over 1000 min, consistent with the OPV based on the InAs CQD ETL (Figure 5b and Table S12, Supporting Information). These results suggest that the photocatalytic effect and photo-oxidation are effectively blocked by the formation of the densely-packed InAs CQD layer on ZnO (Figure S25, Supporting Information). To highlight the high device performance, air- and photo-stability of the nonencapsulated InAs CQD-based PM6:Y6 BHJ OPVs, achieved in this study, we provide the summary of device information, efficiency, and stability of the inverted BHJ OPVs based on NFAs, reported so far (Table S13, Supporting Information).

We carried out incident light intensity (P_{in})-dependent V_{OC} and J_{SC} measurements to evaluate the charge recombination process of InAs CQD-based PM6:Y6 OPVs in detail (Figure 5c,d). All of the charge carriers recombine inside the PM6:Y6 BHJ absorber under open-circuit conditions, and thus the recombination process can be determined by calculating the slope from the relation between V_{OC} and P_{in} (see Experimental procedures details). A slope close to $2kT/q$ indicates that trap-assisted recombination dominates, whereas a slope close to kT/q indicates that bimolecular (i.e., trap-free) recombination dominates (where k is the Boltzmann constant, T is the temperature, and q is the elementary charge at room temperature).^[29] The slopes of OPVs based on ZnO, InAs CQD@ZnO, and InAs CQD ETLs were calculated to be $1.84 kT/q$, $1.73 kT/q$, and $1.19 kT/q$, respectively. These results suggest that V_{OC} decreased due to the slow charge transfer within InAs CQD ETL as confirmed in Figure 3, but the trap-assisted recombination was suppressed by using the InAs CQD ETL with a low trap density (Figure 5c and Figure S30, Supporting Information). J_{SC} also follows a power-law dependence on P_{in} ($J_{SC} \propto P_{in}^\alpha$, where α is the power factor) and, when α is close to 1, the charge carriers are efficiently extracted before bimolecular recombination occurs.^[31] All devices showed linear characteristics of J_{SC} versus P_{in} with the same value of $\alpha = 0.99$, suggesting negligible bimolecular recombination under short-circuit conditions (Figure 5d). In addition, the InAs CQD ETL showed higher electron mobility and lower trap density than the ZnO and SnO₂

ETLs, which were confirmed through the space-charge-limited current (SCLC) fitting of the electron-only devices (Figure S30, Supporting Information).

3. Conclusion

In conclusion, we demonstrated that InAs CQD solids can be employed as an ETL in PM6:Y6 BHJ OPVs and lead to high-efficiency, air- and photo-stable devices under continuous 1 sun illumination without encapsulation technology. Narrow-gap InAs CQD ETLs not only support efficient electron extraction by forming an appropriate energy level to match the LUMO level of NFA Y6, but also effectively suppress detrimental chemical reactions on solar absorber associated with high energy photon. These results were confirmed by various experimental analyses and TMM optical simulations. Based on these findings, bi-layered InAs CQD@ZnO ETLs were devised and achieved a PCE of 15.1% and a Newport-certified PCE of 13.1% in PM6:Y6 BHJ OPVs with high device stability, retaining over 80% of original PCE under continuous 1 sun illumination over 1000 min in ambient air. Our approach based on narrow-gap, density of states tuned CQD based ETLs will provide a versatile and robust method to significantly improve the device stability of thin-film solar cells under real operating conditions with continuous 1 sun illumination in ambient air.

4. Experimental Section

Preparation of ZnO, SnO₂, and InAs CQD ETLs: The sol-gel-derived ZnO precursor solution was prepared by dissolving zinc acetate dihydrate (500 mg) and ethanolamine (0.14 mL) in 2-methoxyethanol (5 mL) under stirring for 6 h at room temperature. ZnO ETL was fabricated by spin-coating the sol-gel-derived ZnO solution on the substrates at 3000 rpm for 30 s and annealed at 200 °C for 30 min in ambient air. To fabricate SnO₂ ETL, the stock solution of SnO₂ nanoparticle (2.5 wt%) diluted to 0.4 wt% in isopropyl alcohol was spin-coated on the substrates at 3000 rpm for 30 s and annealed at 150 °C for 30 min in ambient air. The oleate-capped InAs CQDs, which have an excitonic peak at 1100 nm, were synthesized and their post-treatment with nitrosyl tetrafluoroborate (NOBF₄) for removal of surface ligands was carried out following the methods previously reported.^[41,66] For the ligand passivation of InAs CQDs, solid state ligand-exchange process was performed.^[41] Briefly, the NOBF₄-treated InAs CQDs dispersed in dimethylformamide were spin-coated onto the substrates at 4000 rpm for 30 s. Subsequently, the InAs CQD solids were annealed at 60 °C for 10 min. Then, the InAs CQD solids were fully covered by 0.01 vol% of ammonium chloride solution in methanol (MeOH) for 30 s, followed by washing with neat MeOH three times.

Solar Cell Fabrication: PM6:Y6 bulk-heterojunction OPV (BHJ OPV) was fabricated with inverted structure of indium tin oxide (ITO)/ETL/PM6:Y6/MoO_x/Ag. The ITO substrates were washed with ultrasonication in acetone and isopropyl alcohol sequentially 20 min in each step and dried with air-blower, and then dried in oven for 1 h. Each ETL was fabricated on the cleaned ITO substrates as mentioned above. With the mass ratio of 1:1.2 (14 mg mL⁻¹), PM6:Y6 BHJ solution in chloroform was prepared with the solvent additive of 0.5 vol% 1-chloronaphthalene, and spin-coated at 3000 rpm for 30 s under N₂-filled glove box. After thermal annealing at 90 °C for 10 min in N₂-filled glove box, the PM6:Y6 BHJs on the substrates were transferred to thermal evaporator. Finally, MoO_x (7 nm) and Ag electrode (120 nm) were sequentially deposited by thermal evaporator with patterned shadow mask.

Solar Cell Measurement: Current density–voltage (J – V) curves of PM6:Y6 BHJ OPVs were carried out under a simulated air mass 1.5 global spectrum (AM 1.5G) and 100 mW cm⁻² illumination (1 sun) using a Newport Oriel Sol3A solar simulator with a xenon lamp and a Keithley 2400 sourcemeter. External quantum efficiency (EQE) spectra were measured using a Newport Oriel QuantX300 with an Oriel Cornerstone 130 monochromator. Incident light intensity (P_{in})-dependent open-circuit voltage (V_{oc}) was extracted using the following equation:

$$V_{oc}(P_{in}) = \frac{nkT}{q} \ln(P_{in}) + C \quad (1)$$

Here, n is the ideal factor, k is the Boltzmann's constant, T is the temperature, q is the elementary charge at room temperature, and C is the fitting parameters.

Other Measurement: Absorbance spectra were measured by UV–vis–NIR spectrophotometer (Shimadzu, UV3600). All samples were irradiated under 1 sun illumination in ambient air, while irradiating the light from the glass substrates, and measured for 90 min at 15 min intervals. UV photoelectron spectroscopy (PHI5000 VersaProbe) was used to characterize the energy levels of InAs CQD solids. It was performed using photon lines of He I (21.22 eV), from a discharge lamp. Fermi energy level (E_f) was calculated by following equation: $E_f = 21.22$ eV (the energy of He I UV) – E_{cutoff} (in secondary cutoff region). The VB maximum (E_v) was estimated from semilogarithmic extrapolation in valence-band region, which indicates ($E_v - E_f$). The conduction band minimum positions (E_c) were estimated by adding an energy of excitonic peak of 1.15 eV determined from absorption spectra. FT-IR spectra were measured using a Thermo Scientific Nicolet6700 spectrometer. The work function (W_f) of ZnO, SnO₂, and InAs CQDs solids were measured by APS04 (KP Technology) in ambient air condition. Calibration of the tip W_f was done by measuring W_f of gold substrate before thin film analysis. For the UV illumination, 300-nm laser light was used. Film morphologies and height profiles were measured using AFM in tapping mode, XE-100 from Park Systems. Current–voltage (I – V) curves of electron-only devices were measured using a Keithley 2400 sourcemeter, kept in a dark and inert N₂ condition. The electron-only devices in this study were fabricated with the configuration of ITO/ETLs/PM6:Y6 BHJ/LiF/Al. SCLC fitting was carried out to obtain the trap density (N) and trap-filled limited voltage (V_{TFL}) of ZnO, SnO₂, and InAs CQD ETLs in the respective electron-only devices following the equation:^[67,68]

$$N = \frac{2\epsilon\epsilon_0}{eL^2} V_{TFL} \quad (2)$$

Here, ϵ is the dielectric constant of ZnO ($\epsilon = 8.0$),^[69] SnO₂ ($\epsilon = 3.1$),^[70] and InAs CQD solids ($\epsilon = 10.6$).^[71] ϵ_0 is the vacuum permittivity, e is the amount of coulombic charge of electrons, and L is the thickness of ETLs. Top view scanning electron microscopy (SEM) images were taken using an S-4800 Hitachi. TA spectra were recorded using a commercial TA spectrometer (HELIOS, Ultrafast Systems). Femtosecond Ti:sapphire regenerative amplifier system with 1-kHz repetition rate (Legend, Coherent) and optical parametric amplifier (TOPAS-OPA, Coherent) were used to produce 550-nm and 750-nm pump pulses with power densities of 1.84 and 3.175 μJ cm⁻², respectively. The intensity of pumping lasers was adjusted similarly to solar irradiation of 1 sun to obtain operando condition.^[72] Visible white-light-continuum, probe pulse, was generated by focusing a portion of amplifier output into a sapphire crystal and detected using a multichannel spectrometer with a CMOS sensor.

Optical simulation of PM6:Y6 OPVs: To simulate PM6:Y6 BHJ OPV, the refractive index (n) and absorption coefficient (k) of each layer were measured by ellipsometer (M2000D, Woollam Model Co.) (Figure S31, Supporting Information). Then, the TMM was conducted by MATLAB program to calculate the optical absorption and photocurrent of OPV.^[59] To investigate the ETL thickness-dependent light absorption and generated photocurrent (J_{ph}), the film thickness of ZnO and InAs CQD ETLs was varied from 10 to 50 nm in the TMM simulation. The film thicknesses of ITO, PM6:Y6 BHJ, and metal electrode in this TMM simulation were fixed with 150, 100, and 100 nm respectively. After TMM

calculation, the J_{ph} was evaluated by multiplying the obtained quantum efficiency values by photon flux for the AM 1.5G spectrum.

Supporting Information

Supporting Information is available from the Wiley Online Library or from the author.

Acknowledgements

This work was supported by the National Research Foundation of Korea (NRF-2020R1C1C1003214, NRF-2018R1C1B6001015, NRF-2019R1A2C1086262, NRF-2021R1C1C1005093) grant funded by the Ministry of Science and ICT (MSIT) (NRF-2016R1A5A1012966, NRF-2020M3H4A3081815) and Creative Materials Discovery Program (NRF-2019M3D1A1078299). This work was also funded by National Research Foundation of Korea (Grants NRF-2020R1A4A1018163) under the program of Basic Research Laboratory (BRL).

Conflict of Interest

The authors declare no conflict of interest.

Author Contributions

Y.P., S.Y.B. and T.K. contributed equally to this work. Y.P., S.Y.B., T.K., J.H.S., S.J., and Y.K. discussed the results and prepared the manuscript. Y.P. and S.Y.B. fabricated and characterized the device. T.K. performed the optical simulation. Y.P., S.P., and D.C.L. optimized the synthesis of InAs CQDs. Y.P., S.Y.B., M.C., and D.S. carried out the optical, chemical, and electrical analysis. H.K. and B.K. performed TA measurement and analysis. J.H.S., H.C., S.H.J., and Y.K. supervised the project. All authors have given approval to the final version of the manuscript.

Data Availability Statement

Research data are not shared.

Keywords

device stability, electron transport layers, InAs quantum dots, narrow-gap, organic photovoltaics

Received: December 24, 2021

Revised: April 4, 2022

Published online: May 6, 2022

- [1] M. Jeong, I. Choi, E. M. Go, Y. Cho, M. Kim, B. Lee, S. Jeong, Y. Jo, H. W. Choi, J. Lee, J.-H. Bae, S. K. Kwak, D. S. Kim, C. Yang, *Science* **2020**, *25*, 1615.
- [2] E. H. Jung, N. J. Jeon, E. Y. Park, C. S. Moon, T. J. Shin, T.-Y. Yang, J. H. Noh, J. Seo, *Nature* **2019**, *567*, 511.
- [3] S.-W. Baek, S. Jun, B. Kim, A. H. Proppe, O. Ouellette, O. Voznyy, C. Kim, J. Kim, G. Walters, J. H. Song, S. Jeong, H. R. Byun, M. S. Jeong, S. Hoogland, F. P. García de Arquer, S. O. Kelly, J.-Y. Lee, E. H. Sargent, *Nat. Energy* **2019**, *4*, 969.
- [4] B. Sun, A. Johnston, C. Xu, M. Wei, Z. Huang, Z. Jiang, H. Zhou, Y. Gao, Y. Dong, O. Ouellette, X. Zheng, J. Liu, M.-J. Choi, Y. Gao,

- S.-W. Baek, F. Laquai, O. M. Bakr, D. Ban, O. Voznyy, F. P. García de Arquer, E. H. Sargent, *Joule* **2020**, *4*, 1542.
- [5] L. Meng, Y. Zhang, X. Wan, C. Li, Y. Wang, X. Ke, Z. Xiao, L. Ding, R. Xia, H.-L. Yip, Y. Cao, Y. Chen, *Science* **2018**, *14*, 1094.
- [6] C. Zhu, J. Yuan, F. Cai, L. Meng, H. Zhang, H. Chen, J. Li, B. Qiu, H. Peng, S. Chen, J. Li, B. Qiu, H. Peng, S. Chen, Y. Hu, C. Yang, F. Gao, Y. Zou, Y. Li, *Energy Environ. Sci.* **2020**, *13*, 2459.
- [7] Best research-cell efficiencies; NREL, <https://www.nrel.gov/pv/cell-efficiency.html>, (accessed: November 2021).
- [8] D. Baran, R. S. Ashraf, D. A. Hanifi, M. Abdelsamie, N. Gasparini, J. A. Röhr, S. Holliday, A. Wadsworth, S. Lockett, M. Neophytou, C. J. M. Emmott, J. Nelson, C. J. Brabec, A. Amassian, A. Salleo, T. Kirchartz, J. R. Durrant, I. McCulloch, *Nat. Mater.* **2017**, *16*, 363.
- [9] T. Leijtens, G. E. Eperon, N. K. Noel, S. N. Habisreutinger, A. Petrozza, H. J. Snaith, *Adv. Energy Mater.* **2015**, *5*, 1500963.
- [10] N. Li, J. D. Perea, T. Kassar, M. Richter, T. Heumueller, G. J. Matt, Y. Hou, N. S. Güldal, H. Chen, S. Chen, S. Langner, M. Berlinghof, T. Unruh, C. J. Brabec, *Nat. Commun.* **2017**, *8*, 14541.
- [11] R. Yu, H. Yao, L. Hong, Y. Qin, J. Zhu, Y. Cui, S. Li, J. Hou, *Nat. Commun.* **2018**, *9*, 4645.
- [12] M. Prosa, M. Tassarolo, M. Bolognesi, O. Margeat, D. Gedefaw, M. Gaceur, C. Vidolot-Ackermann, M. R. Andersson, M. Muccini, M. Seri, J. Ackermann, *ACS Appl. Mater. Interfaces* **2016**, *8*, 1635.
- [13] Y. Wang, J. Han, L. Cai, N. Li, Z. Li, F. Zhu, *J. Mater. Chem. A* **2020**, *8*, 21255.
- [14] W. Chen, Y. Wu, Y. Yue, J. Liu, W. Zhang, X. Yang, H. Chen, E. Bi, I. Ashraf, M. Grätzel, L. Han, *Science* **2015**, *350*, 944.
- [15] F. Matteocci, L. Cinà, E. Lamanna, S. Cacovich, G. Divitini, P. A. Midgley, C. Ducati, A. D. Carlo, *Nano Energy* **2016**, *30*, 162.
- [16] D. Ouyang, Z. Huang, W. C. H. Choy, *Adv. Funct. Mater.* **2019**, *29*, 1804660.
- [17] S. S. Shin, S. J. Lee, S. I. Seok, *Adv. Funct. Mater.* **2019**, *29*, 1900455.
- [18] S. O. Oseni, G. T. Mola, *Sol. Energy Mater. Sol. Cells* **2017**, *160*, 241.
- [19] R. Sorrentino, E. Kozma, S. Luzzati, R. Po, *Energy Environ. Sci.* **2021**, *14*, 180.
- [20] J. Yuan, Y. Zhang, L. Zhou, G. Zhang, H.-L. Yip, T.-K. Lau, X. Lu, C. Zhu, H. Peng, P. A. Johnson, M. Leclerc, Y. Cao, J. Ulanski, Y. Li, Y. Zou, *Joule* **2019**, *3*, 1140.
- [21] D. Li, L. Zhu, X. Liu, W. Xiao, J. Yang, R. Ma, L. Ding, F. Liu, C. Duan, F. Fahlman, Q. Bao, *Adv. Mater.* **2020**, *32*, 2002344.
- [22] L. Zhu, M. Zhang, G. Zhou, T. Hao, J. Xu, J. Wang, C. Qiu, N. Prine, J. Ali, W. Feng, X. Gu, Z. Ma, Z. Tang, H. Zhu, L. Ying, Y. Zhang, F. Liu, *Adv. Energy Mater.* **2020**, *10*, 1904234.
- [23] C. Li, J. Zhou, J. Song, J. Xu, H. Zhang, X. Zhang, J. Guo, L. Zhu, D. Wei, G. Han, J. Min, Y. Zhang, Z. Xie, Y. Yi, H. Yan, F. Gao, F. Liu, Y. Sun, *Nat. Energy* **2021**, *6*, 605.
- [24] X. Xu, J. Xiao, G. Zhang, L. Wei, X. Jiao, H.-L. Yip, Y. Cao, *Sci. Bull.* **2020**, *65*, 208.
- [25] R. Sun, W. Wang, H. Yu, Z. Chen, X. Xia, H. Shen, J. Guo, M. Shi, Y. Zheng, Y. Wu, W. Yang, T. Wang, Q. Wu, Y. (Michael) Yang, X. Lu, J. Xia, C. J. Brabec, H. Yan, Y. Li, J. Min, *Joule* **2021**, *5*, 1548.
- [26] H. Chen, H. Lai, Z. Chen, Y. Zhu, H. Wang, L. Han, Y. Zhang, F. He, *Angew. Chem., Int. Ed.* **2021**, *60*, 3238.
- [27] S. Park, H. J. Son, *J. Mater. Chem. A* **2019**, *7*, 25830.
- [28] J. Guo, Y. Wu, R. Sun, W. Wang, J. Guo, Q. Wu, X. Tang, C. Sun, Z. Luo, K. Chang, Z. Zhang, J. Yuan, T. Li, W. Tang, E. Zhou, Z. Xiao, L. Ding, Y. Zou, X. Zhan, C. Yang, Z. Li, C. J. Brabec, Y. Li, J. Min, *J. Mater. Chem. A* **2019**, *7*, 25088.
- [29] J. B. Patel, P. Tiwana, N. Seidler, G. E. Morse, O. R. Lozman, M. B. Johnston, L. M. Herz, *ACS Appl. Mater. Interfaces* **2019**, *11*, 21543.
- [30] E. Hwang, H. Kim, S.-H. Lee, J. H. Seo, H.-T. Kim, C. Lee, S.-Y. Jang, K. Seo, T.-H. Kwon, *Adv. Energy Mater.* **2020**, *10*, 2001238.
- [31] J. Song, C. Li, L. Zhu, J. Guo, J. Xu, X. Zhang, K. Weng, K. Zhang, J. Min, X. Hao, Y. Zhang, F. Liu, Y. Sun, *Adv. Mater.* **2019**, *31*, 1905645.
- [32] M. Cui, D. Li, X. Du, N. Li, Q. Rong, N. Li, L. Shui, G. Zhou, X. Wang, C. J. Brabec, L. A. Nian, *Adv. Mater.* **2020**, *32*, 2002973.
- [33] Kushwaha, M. A., *J. Appl. Phys.* **2012**, *112*, 054316.
- [34] L. Liu, Z. Mei, A. Tang, A. Azarov, A. Kuznetsov, Q.-K. Xue, X. Du, *Phys. Rev. B* **2016**, *93*, 235305.
- [35] F. Kayaci, S. Vempati, I. Donmez, N. Biyikli, T. Uyar, *Nanoscale* **2014**, *6*, 10224.
- [36] K. Bandopadhyay, J. Mitra, *RSC Adv.* **2015**, *5*, 23540.
- [37] G. Tamirat, J. Rick, A. A. Dubale, W.-N. Su, B.-J. Hwang, *Nanoscale Horiz.* **2016**, *1*, 243.
- [38] S. Kim, M. A. M. Rashid, T. Ko, K. Ahn, Y. Shin, S. Nah, M. H. Kim, B. S. Kim, K. Kwak, M. Cho, *J. Phys. Chem. C* **2020**, *124*, 2762.
- [39] T. Kim, S. Park, S. Jeong, *Nat. Commun.* **2021**, *12*, 3013.
- [40] Y. Kim, J. H. Chang, H. Choi, Y.-H. Kim, W. K. Bae, S. Jeong, *Chem. Sci.* **2020**, *11*, 913.
- [41] J. H. Song, H. Choi, H. T. Pham, S. Jeong, *Nat. Commun.* **2018**, *9*, 4267.
- [42] Kudo, Y. M., *Chem. Soc. Rev.* **2009**, *38*, 253.
- [43] X. Wang, F. Wang, Y. Sang, H. Liu, *Adv. Energy Mater.* **2017**, *7*, 1700473.
- [44] W. Ke, G. Fang, Q. Liu, L. Xiong, P. Qin, H. Tao, J. Wang, H. Lei, B. Li, J. Wan, G. Yang, Y. Yan, *J. Am. Chem. Soc.* **2015**, *137*, 6730.
- [45] S. Trost, A. Behrendt, T. Becker, A. Polywka, P. Görrn, T. Riedl, *Adv. Energy Mater.* **2015**, *5*, 1500277.
- [46] Y. Jiang, L. Sun, F. Jiang, C. Xie, L. Hu, X. Dong, F. Qin, T. Liu, L. Hu, X. Jiang, Y. Zhou, *Mater. Horiz.* **2019**, *6*, 1438.
- [47] T. Wang, R. Sun, M. Shi, F. Pan, Z. Hu, F. Huang, F. Li, J. Min, *Adv. Energy Mater.* **2020**, *10*, 2000590.
- [48] E. M. Speller, A. J. Clarke, N. Aristidou, M. F. Wyatt, L. Francàs, G. Fish, H. Cha, H. K. H. Lee, J. Luke, A. Wadsworth, A. D. Evans, I. McCulloch, J.-S. Kim, S. A. Haque, J. R. Durrant, S. D. Dimitrov, W. C. Tsoi, Z. Li, *ACS Energy Lett.* **2019**, *4*, 846.
- [49] Y. Choi, J. W. Jo, F. P. García de Arquer, Y.-B. Zhao, B. Sun, J. Kim, M.-J. Choi, S.-W. Baek, A. H. Proppe, A. Seifitokaldani, D.-H. Nam, P. Li, O. Ouellette, Y. Kim, O. Voznyy, S. Hoogland, S. O. Kelley, Z.-H. Lu, E. H. Sargent, *Adv. Mater.* **2018**, *30*, 1801720.
- [50] S. Bai, Y. Jin, X. Liang, Z. Ye, Z. Wu, B. Sun, Z. Ma, Z. Tang, J. Wang, U. Würfel, F. Gao, F. Zhang, *Adv. Energy Mater.* **2015**, *5*, 1401606.
- [51] G. Lakhwani, R. F. H. Roijmans, A. J. Kronemeijer, J. Gilot, R. A. J. Janssen, S. C. Meskers, *J. Phys. Chem. C* **2020**, *114*, 14804.
- [52] M. Raoufi, U. Hörmann, G. Ligorio, J. Hildebrandt, M. Pätz, T. Schultz, L. Perdigon, N. Koch, E. List-Kratochvil, S. Hecht, D. Neher, *Phys. Status Solidi A* **2020**, *217*, 1900876.
- [53] T. Vai, V. L. Kuznetsov, J. R. Dilworth, P. P. Edwards, *J. Mater. Chem. C* **2014**, *2*, 9643.
- [54] Y. Wang, Q. Fan, X. Guo, W. Li, B. Guo, W. Su, X. Ou, M. Zhang, *J. Mater. Chem. A* **2017**, *5*, 22180.
- [55] N. Ahmad, L. Yanxun, X. Zhang, B. Wang, Y. Zhang, H. Zhou, *J. Mater. Chem. C* **2020**, *8*, 15795.
- [56] B. Matheson, S. J. Pearson, A. Ruseckas, D. W. Samuel, *J. Phys. Chem. Lett.* **2013**, *4*, 4166.
- [57] K. B. Whaley, A. A. Kocherzhenko, A. Nitzan, *J. Phys. Chem. C* **2014**, *118*, 27235.
- [58] G. F. Burkhard, E. T. Hoke, M. D. McGehee, *Adv. Mater.* **2010**, *22*, 3293.
- [59] T. Kim, X. Jin, J. H. Song, S. Jeong, T. Park, *ACS Energy Lett.* **2020**, *5*, 248.
- [60] D. Liu, J. Yang, T. L. Kelly, *J. Am. Chem. Soc.* **2014**, *136*, 17116.
- [61] H. Choi, H. Cho, S. Song, H. Suh, S. Park, J. Y. Kim, *Phys. Chem. Chem. Phys.* **2010**, *12*, 15309.
- [62] C. Goh, S. R. Scully, M. D. McGehee, *J. Appl. Phys.* **2007**, *101*, 114503.

- [63] C. V. Hoven, R. Yang, A. Garcia, V. Crochett, A. J. Heeger, G. C. Bazan, T. Q. Nguyen, *Proc. Natl. Acad. Sci. U. S. A.* **2008**, *105*, 12730.
- [64] P. R. Brown, D. Kim, R. R. Lunt, N. Zhao, M. G. Bawendi, J. C. Grossman, V. Bulović, *ACS Nano* **2014**, *8*, 5863.
- [65] G.-H. Kim, F. P. García de Arquer, Y. J. Yoon, X. Lan, M. Liu, O. Voznyy, Z. Yang, F. Fan, A. H. Ip, P. Kanjanaboos, S. Hoogland, J. Y. Kim, E. H. Sargent, *Nano Lett.* **2015**, *15*, 7691.
- [66] S. Tamang, S. Lee, H. Choi, S. Jeong, *Chem. Mater.* **2016**, *28*, 8119.
- [67] D. Shi, V. Adinolfi, R. Comin, M. Yual, E. Alarousu, A. Buin, Y. Chen, S. Hoogland, A. Rothenberger, K. Katsiev, Y. Losovyj, X. Zhang, P. A. Dowben, O. F. Mohammed, E. H. Sargent, O. M. Bakr, *Science* **2015**, *347*, 519.
- [68] H. F. Haneef, A. M. Zeidell, O. D. Jurchescu, *J. Mater. Chem. C* **2020**, *8*, 759.
- [69] T. J. Bukowski, K. McCarthy, F. McCarthy, G. Teowee, T. P. Alexander, D. R. Uhlmann, J. T. Dawley, B. J. J. Zelinski, *Integr. Ferroelectr.* **1997**, *17*, 339.
- [70] S. Gürakar, T. Serin, N. Serin, *Appl. Surf. Sci.* **2015**, *352*, 16.
- [71] S. Namjoo, A. S. H. Rozatian, I. Jabbari, P. Puschnig, *Phys. Rev. B* **2015**, *91*, 205205.
- [72] J. Guo, H. Ohkita, S. Yokoya, H. Benten, S. Ito, *J. Am. Chem. Soc.* **2010**, *132*, 9631.